Research Article | Open Access

Microstructures

Zhang et al. Microstructures 2026, 6, 20260144 DOI:10.20517/microstructures.2026.208

Directional orthorhombic phase precipitation and coarsening enable strength-ductility synergy in compositionally modified Ti_2AlNb-based alloys

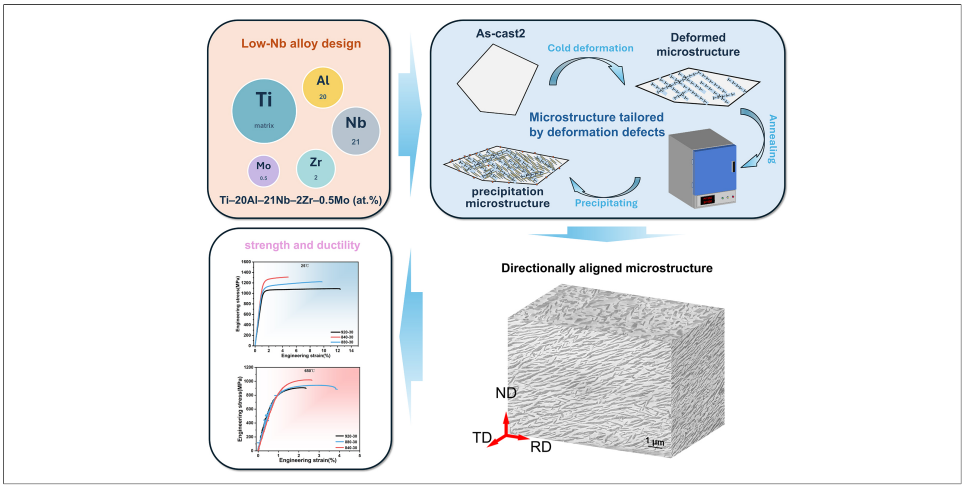
Xu Zhang[1], Yidong Wu[1], Chaohua Li[1], William Yi Wang[2], Xiongjun Liu[1], Xidong Hui[1]

Keywords:
Ti_2AlNb alloy, alloy design, cold rolling, direct aging, O-phase precipitation, strength-ductility synergy

Citation: Zhang, X.; Wu, Y.; Li, C.; Wang, W. Y.; Liu, X.; Hui, X. Directional orthorhombic phase precipitation and coarsening enable strength-ductility synergy in compositionally modified Ti_2AlNb-based alloys. *Microstructures* **2026**, *6*, 20260144. https://dx.doi.org/10.20517/microstructures.2026.208

Received: 30 Jul 2026 **First Decision:** 20 Aug 2026 **Revised:** 13 Sep 2026 **Accepted:** 29 Sep 2026 **Published:** 13 Nov 2026

Academic Editor: Tao Yang
Copy Editor: Ping Zhang
Production Editor: Ping Zhang



Abstract

Ti_2AlNb-based intermetallic alloys are promising candidates for aero-engine hot-end components, yet their intrinsic covalent bonding inevitably causes a strength-ductility trade-off that limits their engineering applications. Herein, a novel strategy integrating directional O-phase precipitation and coarsening is proposed to achieve excellent strength-ductility synergy in newly designed Ti_2AlNb-based alloys. Four alloys with reduced Al and Nb contents were designed, three of which were further modified with Zr and Mo. Among them, the as-cast Ti-20Al-21Nb-2Zr-0.5Mo (A2) alloy exhibited the most favorable tensile performance. Severe cold rolling coupled with short-term direct aging at 880 °C induces the directional precipitation of dense and fine lamellar O-phase. Dislocations and banded substructures provide abundant heterogeneous nucleation sites, while local stress fields and B2/β texture constrain lamellar growth to form a well-aligned microstructure. Prolonged aging primarily enlarges interlamellar spacing, accompanied by a slight decrease in the O-phase area fraction, whereas elevated aging temperatures lead to O-phase coarsening and partial dissolution. These unique microstructural evolutions effectively break the inherent performance bottleneck. The cold-rolled A2 alloy aged at 880 °C for

[1]State Key Laboratory for Advanced Metals and Materials, University of Science and Technology Beijing, Beijing 100083, China
[2]China-Kazakhstan Belt and Road Joint Laboratory on Materials Genome Engineering and Intelligent Science, Northwestern Polytechnical University, Xi'an 710072, Shaanxi, China.

Correspondence to: Prof./Dr. Xidong Hui, Dr. Yidong Wu, State Key Laboratory for Advanced Metals and Materials, University of Science and Technology Beijing, Beijing 100083, China. E-mail: xdhui@ustb.edu.cn; wuyidong@ustb.edu.cn

30 min exhibits superior comprehensive properties, with a room-temperature yield strength of 1,046 MPa, tensile strength of 1,223 MPa, elongation of 9.6%, and a high-temperature tensile strength of 943 MPa at 650 °C, outperforming most previously reported Ti_2AlNb alloys. The coordinated deformation mechanisms stem from concentrated dislocations in B2/β channels and interfacial dislocation pile-ups ensuring high strength, while continuous B2/β channels accommodate plastic strain. This work provides a feasible guideline for composition optimization and short-process manufacturing of high-performance Ti_2AlNb alloys.

INTRODUCTION

Ti_2AlNb-based alloys combine relatively low density and high specific strength with good elevated-temperature strength, creep resistance, and oxidation resistance, making them promising lightweight structural materials for service at 600-750 °C[1,2]. The potential application fields of this kind of alloys include aero-engine compressor disks, blisks, and casings, for which adequate room-temperature ductility needs to coexist with high load-bearing capacity at service temperatures[3]. The ordered intermetallic feature of Ti_2AlNb alloy, however, makes its room-temperature deformation behavior highly sensitive to phase constitution and microstructural morphology. Limited ductility and the intensive tendency toward brittle fracture remain a major challenge to engineering applications[4].

The conflict between the strength and ductility of Ti_2AlNb-based alloys is basically tied to the multiphase microstructure. Ti_2AlNb-based alloys generally are composed of B2/β, O, and α2 phases, among which the B2/β phase accommodates most of the plastic deformation and the O phase provides strength at both room and elevated temperatures[5]. Nevertheless, an excessive O-phase fraction or overly fine O-phase lamellae may restrict dislocation motion in B2/β[6]. Thus it is essential to achieve a balance between the strengthening of O-phase and plastic deformation in B2/β phase for comprehensive high-temperature strength and room-temperature ductility.

Alloy composition governs the stability of the B2/β phase and the tendency for O-phase precipitation, providing the basis for balancing strength and ductility. Previous studies have shown that partially replacing Nb with Zr and adding an appropriate amount of Mo can regulate phase stability and elemental partitioning, thereby improving elevated-temperature performance while maintaining strength and ductility[7]. An appropriate composition establishes the basis for phase-balance control, but it does not determine the final microstructure. The fraction and morphology of O phase must still be adjusted through subsequent processing and heat treatment. As-cast Ti_2AlNb alloys generally contain coarse B2/β grains and exhibit limited room-temperature ductility. Multidirectional isothermal forging, hot rolling, or hot extrusion is therefore commonly employed to refine the microstructure and form the alloy, followed by solution and aging treatments to adjust the fractions and morphologies of B2/β, O, and α_2 phases[8-10]. Fine O-phase lamellae favor high strength, whereas coarse lamellae and a continuous B2/β phase improve ductility[11]. Achieving the desired microstructure, however, usually requires several coupled processing steps and is highly sensitive to the processing parameters. Solution treatment also recovers most of the dislocations introduced during prior deformation and releases the stored deformation energy[12]. In this case, the influence of deformation substructure on the subsequent O-phase precipitation is weakened.

Direct aging after cold deformation without an intervening solution treatment allows the prior deformation substructure to influence subsequent O-phase precipitation, offering a possible route for defect-mediated control of O-phase precipitation. Tang *et al.*[13] found that pre-straining increased the number of favorable nucleation sites and promoted the formation of O-phase clusters at grain boundaries; Zheng *et al.*[14] observed dislocation-induced variant selection and parallel O-phase lamellae. Dislocation structures produced by hot shear spinning were also found to affect O-phase variant selection and lamellar

arrangement[15]. These previous works suggest that deformation defects not only promote precipitation but may also alter its spatial distribution through interactions between local stress fields and transformation strains. However, these effects were mainly examined in localized defect-rich regions or selected parent grains. Moving beyond these localized observations requires examining a deformation state that extends beyond isolated defect-rich regions of the parent phase. Severe cold rolling is relevant in this respect because it introduces a high density of dislocations and shear bands together with a pronounced rolling texture in the B2/β parent phase. Wei *et al.*[16] observed micro-shear bands less than 200 nm thick in a Ti_2AlNb alloy after 80% cold rolling, but did not examine how the resulting deformation state affected O-phase precipitation during subsequent direct aging. Consequently, the relationship between the inherited cold-rolled state, early O-phase precipitation, and directional lamella formation remains insufficiently understood. The broader question is whether this deformation state can be exploited during direct aging to construct a broadly distributed O/B2 microstructure and thereby regulate tensile properties.

The present study aims to achieve a favorable strength-ductility balance by combining composition design with deformation-assisted O-phase precipitation and controlled lamellar coarsening. We used Ti-20Al-23Nb as the reference alloy and designed three Zr- and Mo-modified alloys by partially replacing Nb with Zr and adding a small amount of Mo. Compared with Ti_2AlNb-based alloys, the newly designed alloys contain less Al to improve room-temperature ductility and less Nb to reduce density and raw-material cost. The as-cast microstructures and room-temperature tensile properties of the four alloys were investigated. The optimized alloy was then cold rolled to an 80% thickness reduction and subjected to short-time direct aging without an intermediate solution treatment. Tensile testing at room temperature and 650 °C, along with the fractography, post-tensile substructure characterization, and strengthening-contribution calculations, was used to evaluate the effects of residual dislocations, O-phase lamellae, and B2/β channels on strength and ductility. Unlike the conventional solution-aging route, this route carries the deformation substructure inherited from cold rolling into the aging treatment, allowing it to promote directional O-phase precipitation and influence subsequent lamellar coarsening. In this way, the established defect-assisted precipitation effect is developed into a microstructure-control strategy for tuning the O/B2 architecture and balancing room-temperature ductility with elevated-temperature strength.

MATERIALS AND METHODS

Material preparation

Four Ti_2AlNb-based alloys were designed to combine high strength with good ductility. Their nominal compositions were Ti-20Al-23Nb, Ti-20Al-21Nb-2Zr-0.5Mo, Ti-20Al-19Nb-4Zr-0.5Mo, and Ti-20Al-17Nb-6Zr-0.5Mo, hereafter referred to as A0, A2, A4, and A6, respectively. All compositions are given in at.%. The alloys were produced by non-consumable-electrode vacuum arc melting using a WK-II vacuum arc-melting furnace (Beijing Wuke Optoelectronic Technology Co., Ltd., China) under an argon atmosphere. Before melting the alloy charge, titanium sponge was melted as a getter to lower the residual oxygen level in the furnace chamber. Each ingot was inverted and remelted five times to improve compositional homogeneity. The melt was then suction-cast into a water-cooled copper mold, yielding ingots approximately 10 × 10 × 50 mm^3 in size. After comparing the phase constitution, strength, and tensile ductility of the four alloys in the as-cast condition, A2 was selected for the subsequent cold-rolling and direct-aging experiments. Cold rolling was carried out on a two-high rolling mill. A thickness reduction of 5% was applied in each pass until a total reduction of 80% was reached, without intermediate annealing. The final sheet thickness was 2 mm. The cold-rolled condition is denoted as CR, while RD, TD, and ND refer to the rolling, transverse, and normal directions, respectively. The detailed process of sample preparation is illustrated in Figure 1.

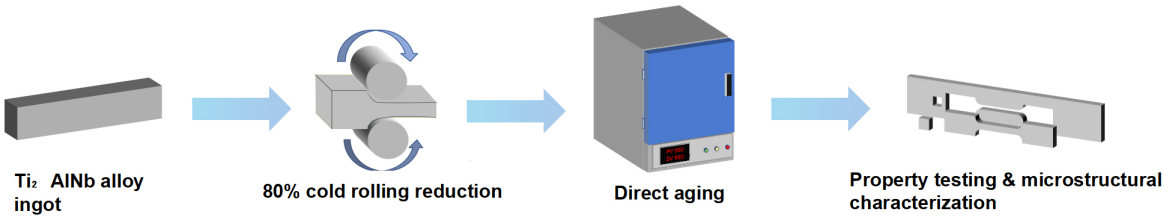


Figure 1. Schematic diagram of the preparation process route.

Direct aging was conducted in a box-type resistance furnace (SXL-1400C, Shanghai Jujing Precision Instrument Manufacturing Co., Ltd., China). All specimens used for aging had identical dimensions of 50 × 7 × 2 mm^3. Before each aging treatment, the furnace was preheated and stabilized at the target temperature. After specimen insertion, the holding time was started only when the furnace temperature indicated by the controller had returned to the target temperature. To evaluate the effect of aging temperature, the cold-rolled specimens were held at 840, 880, and 920 °C for 30 min. These conditions are denoted as T840-30, T880-30, and T920-30, respectively. A separate set of specimens was aged at 880 °C for 2, 5, 10, and 30 min to track the evolution of the O-phase lamellae with time, which are denoted as T880-2, T880-5, T880-10, and T880-30, respectively. To assess the effect of prior cold rolling on O-phase precipitation, an undeformed specimen from the same alloy batch was also aged at 880 °C for 2 min, hereafter referred to as U880-2. After aging, all specimens were immediately water-quenched.

Microstructure characterization

Thermodynamic calculations were performed using Thermo-Calc software (version 2025a, Thermo-Calc Software AB, Sweden) with the TCTi6 thermodynamic database. The nominal alloy compositions were used as input, and equilibrium phase-fraction calculations were conducted as a function of temperature to evaluate the stability and evolution of the constituent phases. The phase constitutions of the as-cast, cold-rolled, and directly aged specimens were analyzed using an X-ray diffractometer (SmartLab SE, Rigaku Corporation, Japan). Patterns were recorded over a 2θ range of 20-100° at a scanning rate of 2°/min. The same instrument was also used to characterize the bulk texture of the B2/β phase in the cold-rolled sheet. Measurements were taken from the rolling direction-transverse direction (RD-TD) plane, and the {110}, {200}, and {211} pole figures were collected. Electron backscatter diffraction (EBSD) was performed using a NordlysMax2 EBSD detector (Oxford Instruments NanoAnalysis, UK) mounted on a JSM-7200F field-emission scanning electron microscope (JEOL Ltd., Japan) to determine the grain morphology and grain size of the as-cast alloys. The microstructures after direct aging were examined using the same field-emission scanning electron microscope (FE-SEM). Before EBSD and Scanning Electron Microscopy (SEM) observations, the specimens were mechanically ground and polished, followed by electropolishing at 25 V using an MS-305D DC power supply (MAISHENG, China). The 1-propanol, 1-butanol, and perchloric acid used to prepare the electrolyte were purchased from Sinopharm Chemical Reagent Co., Ltd., China. The electrolyte contained 60 vol.% 1-propanol, 34 vol.% 1-butanol, and 6 vol.% perchloric acid. Unless otherwise stated, microstructural observations were performed on the rolling direction-normal direction (RD-ND) plane. Transmission electron microscopy was performed using a Talos F200S microscope (Thermo Fisher Scientific, USA) operated at 200 kV. The transmission electron microscopy (TEM) specimens were mechanically ground to a thickness below 50 μm and then ion-milled using a model 691 precision ion polishing system (Gatan, Inc., USA). ImageJ was used for quantitative microstructural analysis. At least five randomly selected fields of view were analyzed for each condition, and the same grayscale thresholding criterion was applied throughout to identify the O-phase-rich regions. The orientation angles of the O-phase lamellae were measured from randomly selected SEM images using ImageJ and grouped into 10° intervals. The orientation angle(θ) was defined as the acute angle between the lamellar long axis and RD. The alignment factor was calculated as[17]:

$$A = \sqrt{\left(\frac{1}{N}\sum_{i=1}^{N}\cos 2\theta_i\right)^2 + \left(\frac{1}{N}\sum_{i=1}^{N}\sin 2\theta_i\right)^2} \quad (1)$$

where N is the total number of measured lamellae. A ranges from 0 for a random distribution to 1 for complete alignment.

Mechanical property testing

Tensile specimens were machined with their tensile axes parallel to the RD, except for the additional TD specimens of T880-30. The specimens tested at room temperature had gauge dimensions of 18 × 3 × 2 mm^3 (length × width × thickness), whereas those used for testing at 650 °C measured 8 × 2 × 2 mm^3. The tensile tests were performed using an LE5105 dual-column electronic universal testing machine [Lishi (Shanghai) Scientific Instruments Co., Ltd., China]. Tests at both temperatures were conducted at an initial strain rate of 1×10^{-3} s^{-1}. Before testing at 650 °C, the specimens were heated at 10 °C min^{-1} and held at the test temperature for 10 min to minimize the temperature gradient along the gauge section.

RESULTS AND DISCUSSION

Composition, microstructure and tensile properties of as-cast alloys

Conventional Ti_2AlNb-based alloys were developed based on Ti-22Al-25Nb and Ti-22Al-27Nb alloys, in which relatively high levels of Nb help to maintain elevated-temperature properties. However, the high Nb content also increases the alloy density and raw-material cost. Simply reducing the Nb content may impair creep resistance and alter the balance between the B2/β and O phases. The alloy design was therefore centered on the B2/β matrix state required for the subsequent processing route. The target was a B2/β-dominated as-cast alloy with sufficient room-temperature deformability to withstand severe cold rolling, while retaining sufficient O-phase stability for precipitation strengthening during direct aging.

In this work, we designed new alloys based on the ternary Ti-20Al-23Nb alloy, in which the Al content was reduced to improve room-temperature ductility, whereas the Nb content was reduced to lower the density and raw-material cost. To satisfy the competing requirements of deformability, phase stability, and elevated-temperature strengthening, a constrained substitution strategy was adopted. For A2, A4, and A6, the combined Nb and Zr content was maintained at 23 at.%, while Zr progressively replaced Nb at 2, 4, and 6 at.%. Zr was introduced to provide solid-solution strengthening and help mitigate the possible loss of creep resistance associated with reduced Nb[7]. Mo was fixed at 0.5 at.% throughout the modified series to compensate for the reduced β-stabilizing effect of Nb and maintain a suitable B2/β-O phase balance[18]. Keeping the Mo content constant also allowed the progressive Zr substitution within A2-A6 to be evaluated without introducing an additional compositional variable. The calculated equilibrium phase-fraction curves [Supplementary Figure 1] showed that the β-transus temperature decreased progressively from A0 to A6, indicating that the B2/β phase remained stable to lower temperatures as the composition was modified. The estimated raw-material costs and theoretical densities of the designed alloys were competitive with those of conventional Ti_2AlNb-based alloys.

The EBSD inverse pole figure maps of the four as-cast alloys are presented in Figure 2. All four alloys exhibited equiaxed grains, while their average grain size decreased from 176 to 110 μm with increasing Zr content. The accompanying grain refinement may provide an additional strengthening contribution. The X-ray diffraction (XRD) patterns in Figure 3A show distinct B2/β-phase peaks, whereas no detectable peaks associated with the O or α_2 phase are present. These results indicate that all four as-cast alloys were predominantly B2/β and that the compositional modifications did not cause an obvious change in the as-cast phase constitution. For A2-A6, the retention of a B2/β-dominated as-cast structure despite the progressive reduction in Nb is consistent with the overall design objective of preserving a deformable B2/β parent phase through the combined Zr/Mo modification.

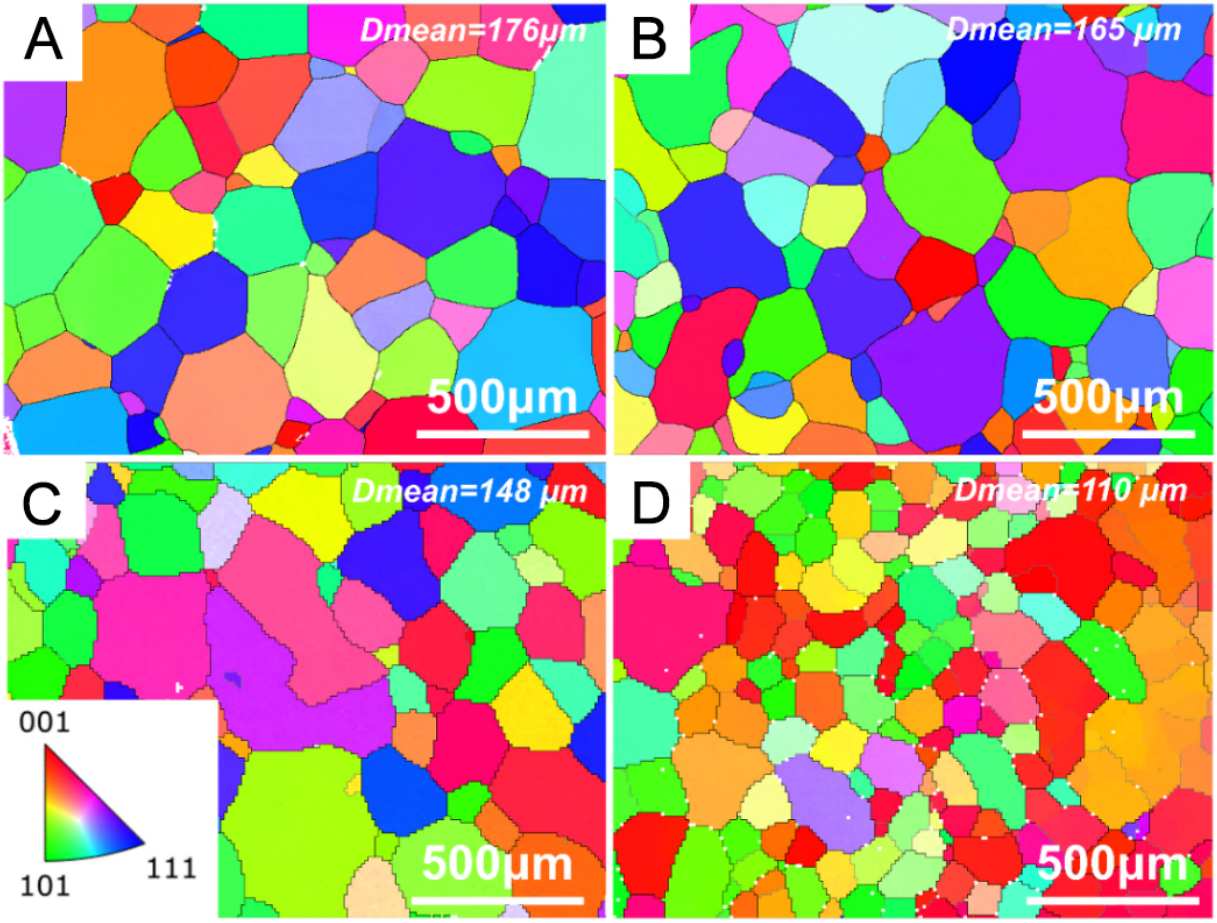


Figure 2. Inverse pole figure (IPF) maps of the as-cast (A) A0, (B) A2, (C) A4, and (D) A6 alloys.

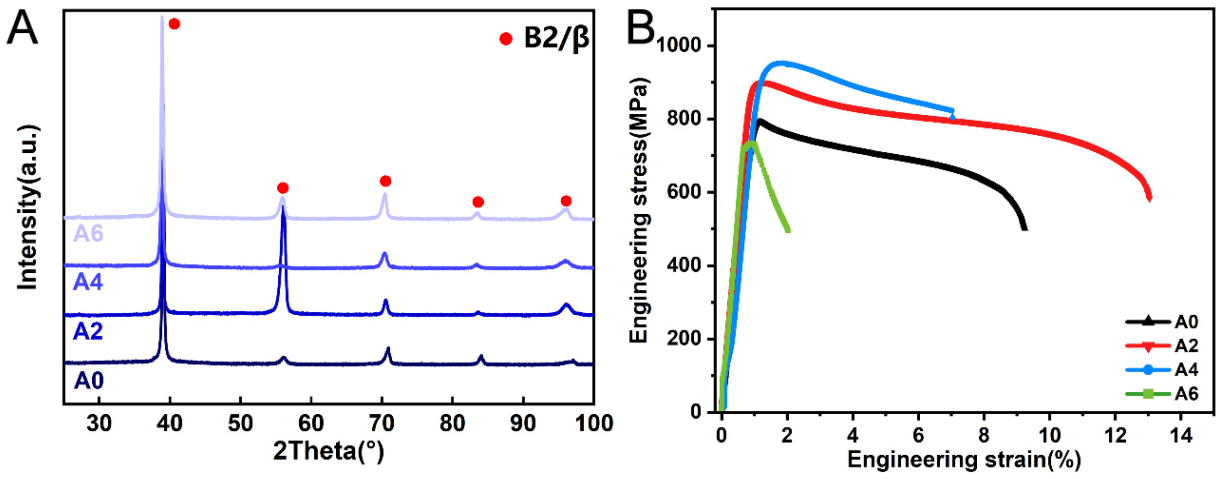


Figure 3. (A) X-ray diffraction (XRD) patterns and (B) engineering stress-strain curves of the as-cast A0, A2, A4, and A6 alloys.

Figure 3B shows the room-temperature engineering stress-strain curves of the four as-cast alloys. A0 reached an ultimate tensile strength of approximately 794 MPa and fractured at an engineering strain of 9.2%. Relative to A0, A2 exhibited both higher strength and greater ductility, with an ultimate tensile strength of approximately 894 MPa and an engineering strain to fracture of 13.2%. With the Mo content fixed at 0.5 at.%

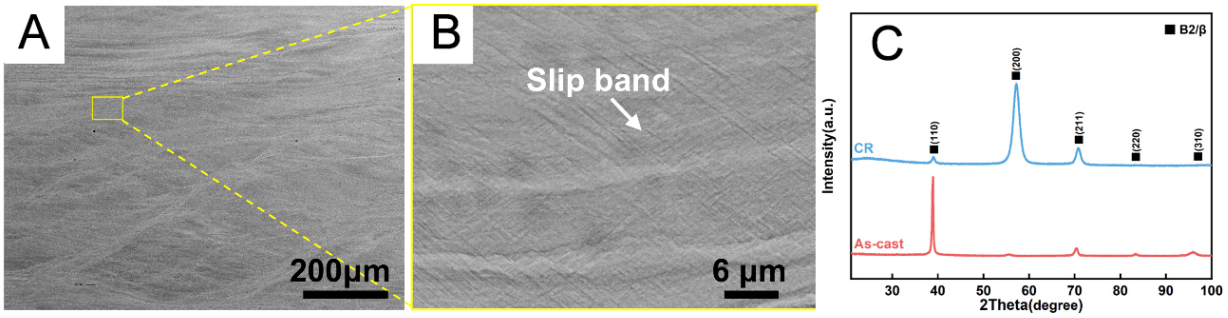


Figure 4. (A and B) Microstructures and (C) X-ray diffraction (XRD) pattern of A2 alloy after 80% cold-rolling deformation.

and the combined Nb and Zr content unchanged, increasing the Zr content from 2 to 4 at.% raised the ultimate tensile strength of A4 to approximately 948 MPa. Its fracture strain, however, fell to about 7.0%. At 6 at.% Zr, the engineering stress of A6 rose to approximately 730 MPa before dropping rapidly, and fracture occurred at only 2.1% strain. Within the composition range investigated, increasing the Zr content did not lead to a continuous improvement in overall tensile performance. Although A4 was slightly stronger than A2, the latter combined a relatively high strength with the highest fracture strain among the four alloys, giving the most favorable strength-ductility balance. The favorable strength-ductility balance of A2 may therefore be related to the combined effects of substitutional solid-solution strengthening and grain refinement, together with the retention of a relatively deformable B2/β-dominated matrix. Considering the as-cast phase constitution, grain structure, and room-temperature tensile properties, Ti-20Al-21Nb-2Zr-0.5Mo(A2) was selected for the subsequent cold-rolling and direct-aging experiments.

Directional precipitation and coarsening of O-phase

Figure 4A and B show the microstructure of the A2 alloy after cold rolling to an 80% thickness reduction. Compared with the equiaxed as-cast microstructure, the grains were severely deformed and elongated along RD, with distinct deformation bands observed within the grains. The XRD pattern in Figure 4C remained dominated by B2/β reflections, with no discernible peaks corresponding to the O or α_2 phase, indicating that cold rolling did not produce a detectable change in the phase constitution. However, several diffraction peaks exhibited noticeable broadening and changes in relative intensity. These variations are consistent with substantial dislocation accumulation and pronounced crystallographic reorientation induced by cold rolling.

To assess the influence of cold deformation on precipitation during short-duration direct aging, Figure 5A and B compare the backscattered electron (BSE) microstructures of an as-cast specimen and an 80% cold-rolled specimen, both aged at 880 °C for 2 min under identical conditions. U880-2 contained only a few sparsely distributed O-phase lamellae, corresponding to an area fraction of approximately 15%; by contrast, T880-2 contained numerous fine lamellae with a much higher area fraction of about 45.4% and a pronounced preferential alignment within the B2/β matrix. Quantitative orientation analysis further showed that 93.6% of the measured lamellae were oriented within 30° of RD, with an alignment factor of 0.809, confirming a strongly concentrated morphological alignment [Supplementary Figure 2]. Discrete granular α_2 particles were also observed along the elongated grain boundaries in T880-2. These observations indicate that prior cold rolling substantially promoted O-phase precipitation during short-duration direct aging and promoted the preferential alignment of the resulting lamellae.

The subsequent evolution of the O-phase lamellae was examined by varying the aging time and temperature. Figure 6A-D show the microstructures of the cold-rolled specimens after aging at 880 °C for 2, 5, 10, and 30 min. Numerous fine O-phase lamellae had already formed in the B2/β matrix after 2 min. On the RD-TD plane, their long axes exhibited a preferred alignment, producing a fine alternating structure with the

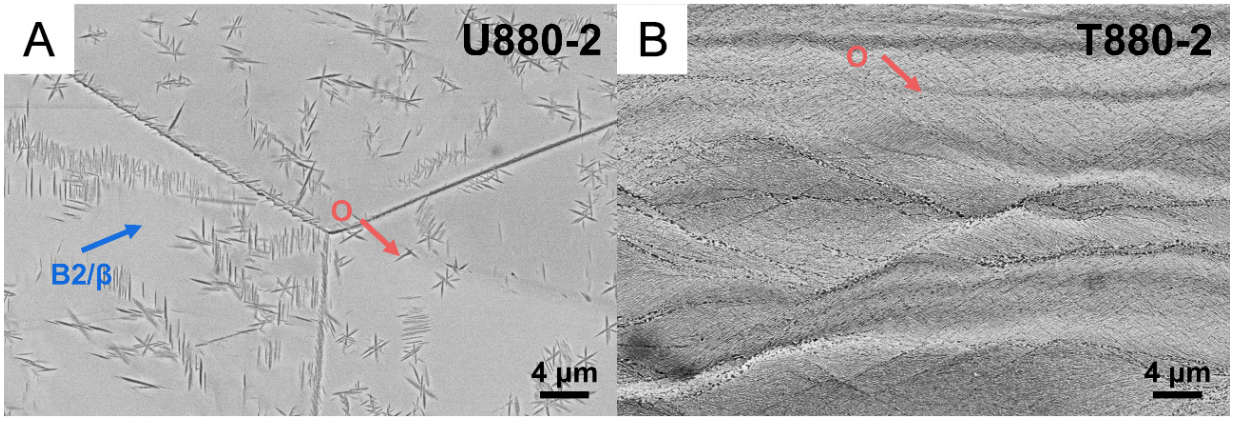


Figure 5. Backscattered electron (BSE) microstructures of the (A) as-cast and (B) cold-rolled A2 alloys after aging at 880 °C for 2 min.

retained B2/β phase. After 5 min, the overall alignment and arrangement of the lamellae remained largely unchanged. Some lamellae, however, began to thicken and became more clearly defined. Further aging to 10 and 30 min led to continued thickening, and the initially fine structure gradually evolved into a coarser lamellar morphology. To assess whether this apparent alignment was specific to the RD-TD plane, T880-30 was additionally examined on the RD-ND and TD-ND planes. The corresponding three-dimensional schematic composite in Supplementary Figure 3 revealed plane-dependent but non-random lamellar arrangements on all three orthogonal sections. The quantitative measurements are summarized in Figure 6E. As the holding time increased from 2 to 30 min, the mean O-phase lamellar thickness increased from 56.8 ± 14.7 to 96.9 ± 33.3 nm, while the interlamellar spacing increased from 49.3 ± 17.5 to 122.5 ± 48.7 nm. In comparison, the area fraction decreased only modestly, from 45.4 ± 2.2% to 40.4 ± 0.8%. Thus, a relatively high O-phase fraction was established within the first 2 min of direct aging, whereas further aging had only a limited effect on the area fraction and mainly resulted in lamellar thickening and increased interlamellar spacing.

Direct-aging temperature also had a pronounced effect on the final O-phase morphology. Figure 7A shows the XRD patterns of the cold-rolled (CR) condition and cold-rolled specimens after aging at 840, 880, and 920 °C for 30 min. All three patterns were dominated by reflections from the B2/β and O phases, together with weaker α_2 reflections. An enlarged view of the 2θ range from 30° to 45° is provided in Figure 7B. As the aging temperature increased, the relative intensities of the O and α_2 phase peaks gradually decreased, suggesting a reduced relative contribution of these phases to the diffraction patterns. The corresponding microstructures are shown in Figure 8. T840-30 contained numerous fine, closely spaced O-phase lamellae, forming a dense alternating O/B2 lamellar structure. At 880 °C, the lamellae became noticeably thicker, and the intervening B2/β regions were more clearly defined. Further coarsening occurred in T920-30. The B2/β channels widened substantially, while the O-phase lamellae became markedly less abundant. Quantitative results in Figure 9 further demonstrate this trend. As the direct-aging temperature increased from 840 to 920 °C, the mean lamellar thickness increased from 71.4 ± 24.0 to 109.8 ± 31.8 nm, and the interlamellar spacing increased from 73.7 ± 24.3 to 230.4 ± 50.4 nm. Over the same temperature range, the O-phase area fraction decreased from 46 ± 1.4% to 14.6 ± 1.3%. This decrease was broadly consistent with the reduced relative intensities of the O-phase reflections in the XRD patterns.

To evaluate the effect of these microstructural changes on tensile behavior, T840-30, T880-30, and T920-30 were tested at room temperature and 650 °C. Figure 10A shows the typical room-temperature engineering stress-strain curves. The statistical tensile results obtained from repeated tests, including the yield strength, ultimate tensile strength, and elongation, are summarized as mean ± standard deviation in

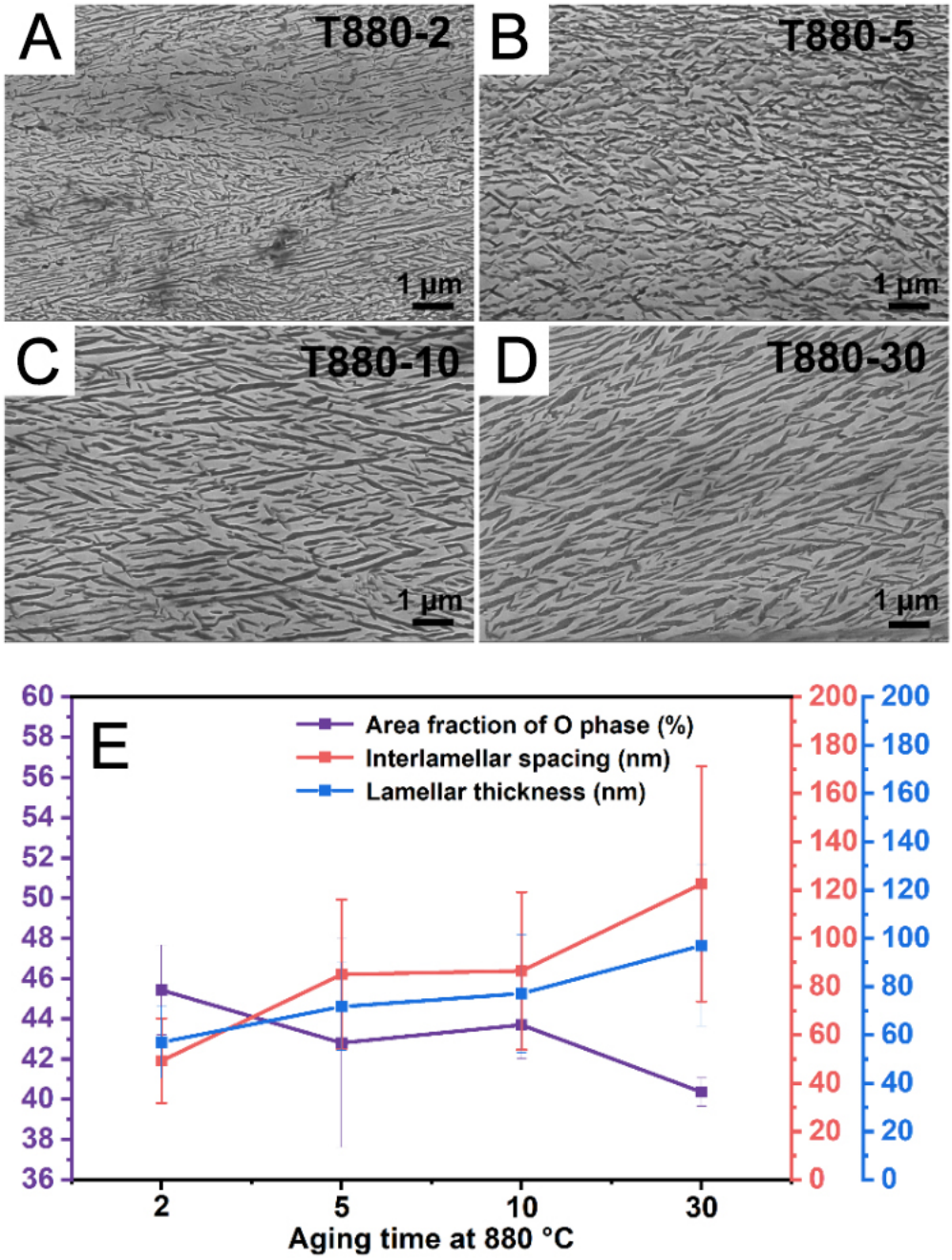


Figure 6. SEM images of the cold-rolled alloy after aging at 880 °C for (A) 2, (B) 5, (C) 10, and (D) 30 min, and (E) statistical charts of the O-phase area fraction, interlamellar spacing, and lamellar thickness. The error bars represent the standard deviation (SD), with n = 5. SEM: Scanning electron microscopy.

Supplementary Table 1. T840-30 exhibited the highest yield strength and ultimate tensile strength, reaching 1,188 and 1,323 MPa, respectively, but its uniform elongation was limited to 4.2%. Raising the direct-aging temperature to 880 °C reduced the corresponding strengths to 1,046 and 1,223 MPa, while increasing the elongation to 9.6%. At 920 °C, the yield strength and ultimate tensile strength decreased further to 981 and 1,096 MPa, with an elongation of 12.3%. The corresponding microstructural parameters and tensile properties are compared in Supplementary Table 2. Overall, the room-temperature tensile response shifted progressively from high strength and low ductility to lower strength and higher ductility as the direct-aging temperature increased. When tested at 650 °C, T840-30, T880-30, and T920-30 exhibited ultimate tensile

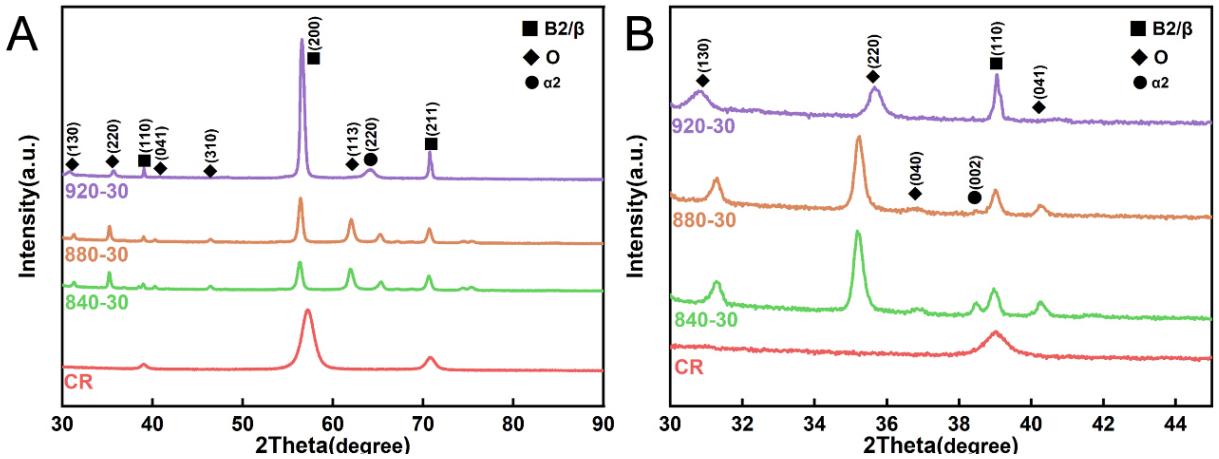


Figure 7. (A) XRD patterns of the cold-rolled alloy and after aging at 840, 880, and 920 °C for 30 min, and (B) the corresponding magnified view in the 2θ range of 30°-45°. XRD: X-ray diffraction.

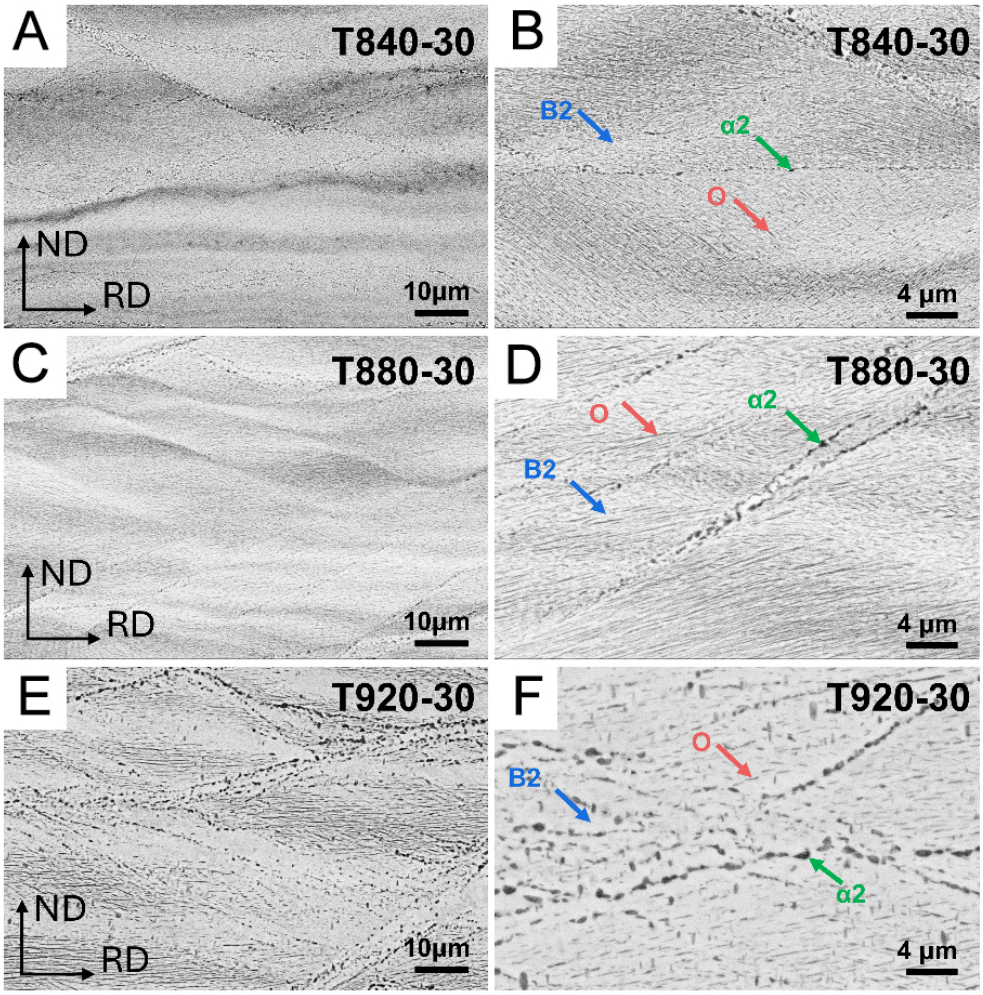


Figure 8. Backscattered electron (BSE) images of the cold-rolled alloy after aging at (A and B) 840, (C and D) 880, and (E and F) 920 °C for 30 min.

strengths of 1,024, 943, and 908 MPa, respectively [Figure 10B]. All three specimens showed lower ultimate tensile strengths than at room temperature. The strength ranking among the three conditions remained the

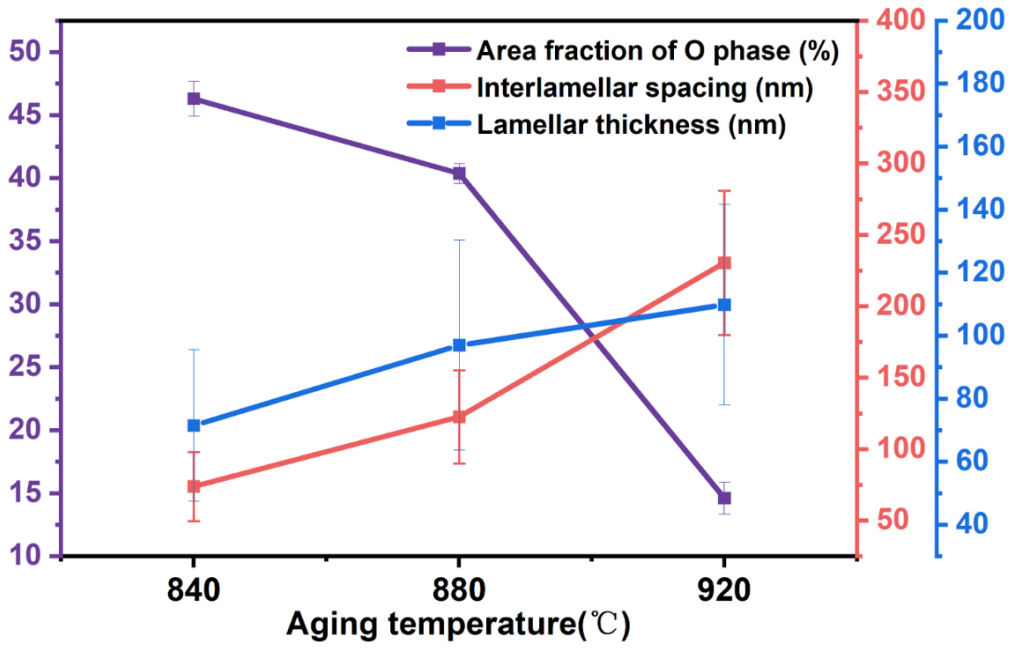


Figure 9. Statistical charts of the O-phase area fraction, interlamellar spacing, and lamellar thickness of the cold-rolled alloy after aging at 840, 880, and 920 °C for 30 min. The error bars represent the standard deviation (SD), with n = 5.

same as that at room temperature. Thus, changing the direct-aging temperature allowed the room-temperature strength-ductility balance to be tuned over a broad range, while all three conditions retained relatively high tensile strength at 650 °C. Considering the pronounced rolling texture and preferentially aligned O-phase lamellae, the tensile response of T880-30 was further examined along TD [Supplementary Figure 4]. The TD specimen showed slightly higher ultimate tensile strength but lower elongation than the RD specimen at both room temperature and 650 °C, indicating that the tensile anisotropy is more pronounced in ductility than in strength.

Figure 10C compares the room-temperature ultimate tensile strength and uniform elongation of the present alloy with those of reported Ti_2AlNb-based alloys fabricated by various processing routes, including forging[19-22], hot rolling[23,24], additive manufacturing (AM)[25-28], and powder metallurgy (PM)[29-31]. All three directly aged conditions lie near the upper range of the reported data. T840-30 falls within the high-strength regime, whereas T880-30 and T920-30 extend toward higher uniform elongations. At comparable uniform elongations, T880-30 and T920-30 retain higher ultimate tensile strengths than most of the reported Ti_2AlNb-based alloys. Figure 10D compares the specific ultimate tensile strength and elongation at 650 °C. The present samples are located in the high-specific-strength region. At comparable elongations, their specific tensile strengths are higher than those of powder-metallurgy-processed and hot-rolled alloys and lie near the upper range reported for forged and additively manufactured alloys. T840-30 occupies the high specific-strength region, while T880-30 combines high specific tensile strength with better high-temperature elongation. Taken together, T880-30 provides a favorable balance of room-temperature strength and ductility while retaining a high specific load-bearing capacity at 650 °C.

Mechanism of deformation-induced directional O-phase precipitation

To understand how cold deformation followed by direct aging produces directionally aligned O-phase lamellae and tunes the strength-ductility balance, the role of the cold-rolling substructure in O-phase precipitation must first be considered. Cold deformation promotes O-phase precipitation primarily by altering the defect state of the B2/β matrix. As shown in Figure 11A-C, an 80% thickness reduction by cold

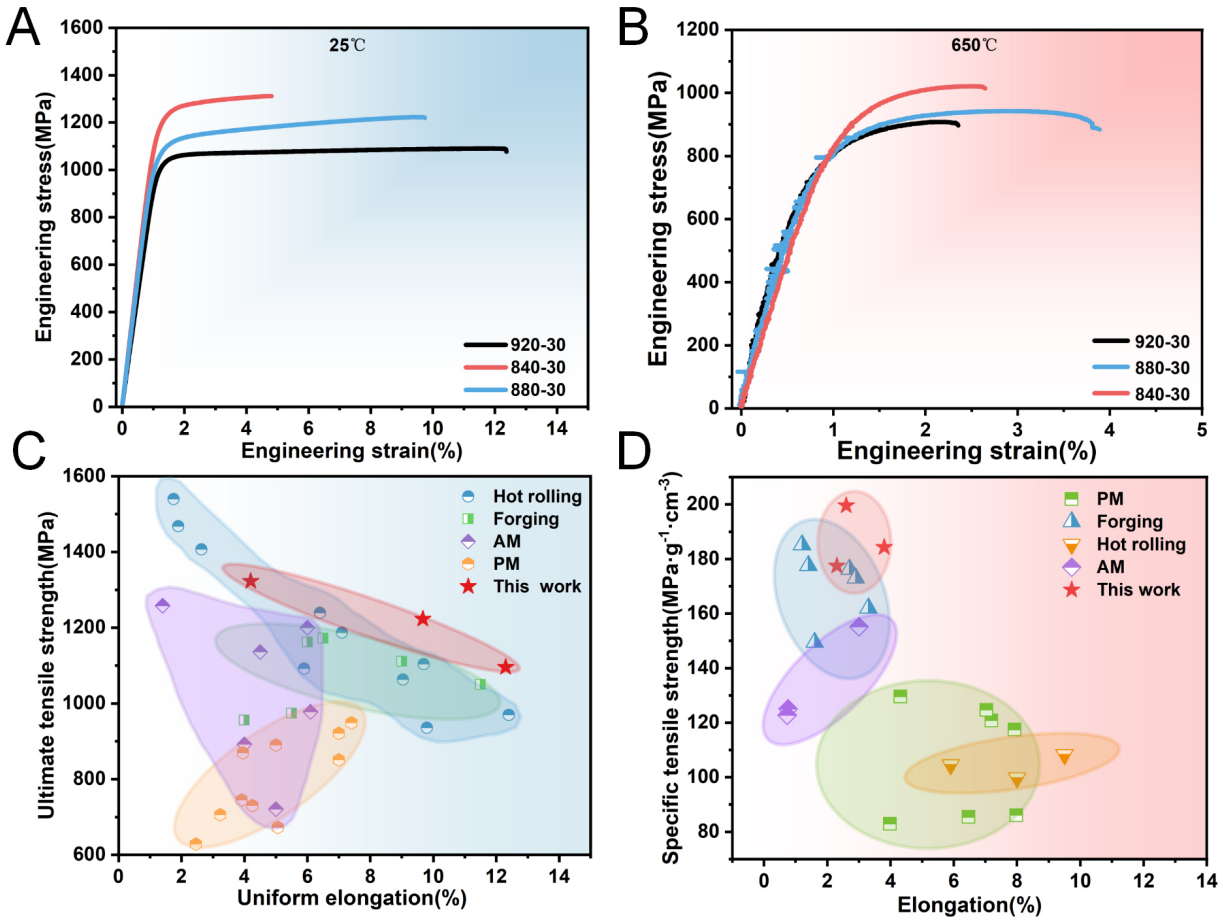


Figure 10. Stress-strain curves (A) at room temperature and (B) at 650 °C for the T840-30, T880-30, and T920-30 specimens; (C) comparison of room-temperature ultimate tensile strength and uniform elongation and (D) comparison of specific ultimate tensile strength and elongation at 650 °C with previously reported Ti_2AlNb-based alloys produced by forging, hot rolling, AM and PM. AM: Additive manufacturing; PM: powder metallurgy.

rolling generated a high density of dislocations, dislocation tangles, and banded deformation substructures. These deformation-induced defects increase the local stored energy and provide numerous heterogeneous nucleation sites for the O phase. The local stress fields associated with dislocations may also partially accommodate the transformation strain associated with O-phase formation, thereby lowering the barrier for nucleation in defect-rich regions. Previous studies have similarly shown that pre-deformation can markedly alter the nucleation behavior and morphology of the O phase in Ti_2AlNb-based alloys, with preferential precipitation often occurring in regions of high dislocation density[13,32]. The high density of deformation defects generated by cold rolling therefore provides a microstructural basis for the enhanced O-phase precipitation during the early stage of direct aging.

Figure 11D-H present the TEM characterization of the T880-2 sample. Dense O-phase lamellae with a pronounced preferential alignment were observed within the B2/β matrix. Selected-area electron diffraction (SAED) confirmed that the precipitates were the orthorhombic O phase. The lamellae appeared bright in the dark-field image obtained using an O-phase reflection and were readily distinguished from the surrounding B2/β matrix in the high-angle annular dark-field (HAADF) image. Energy-dispersive X-ray spectroscopy (EDS) maps further revealed distinct distributions of Al and Nb between the two phases, indicating local solute redistribution. Meanwhile, a high density of dislocations persisted in the B2/β regions between adjacent lamellae. The coexistence of O-phase lamellae and unrecovered dislocations after only 2 min

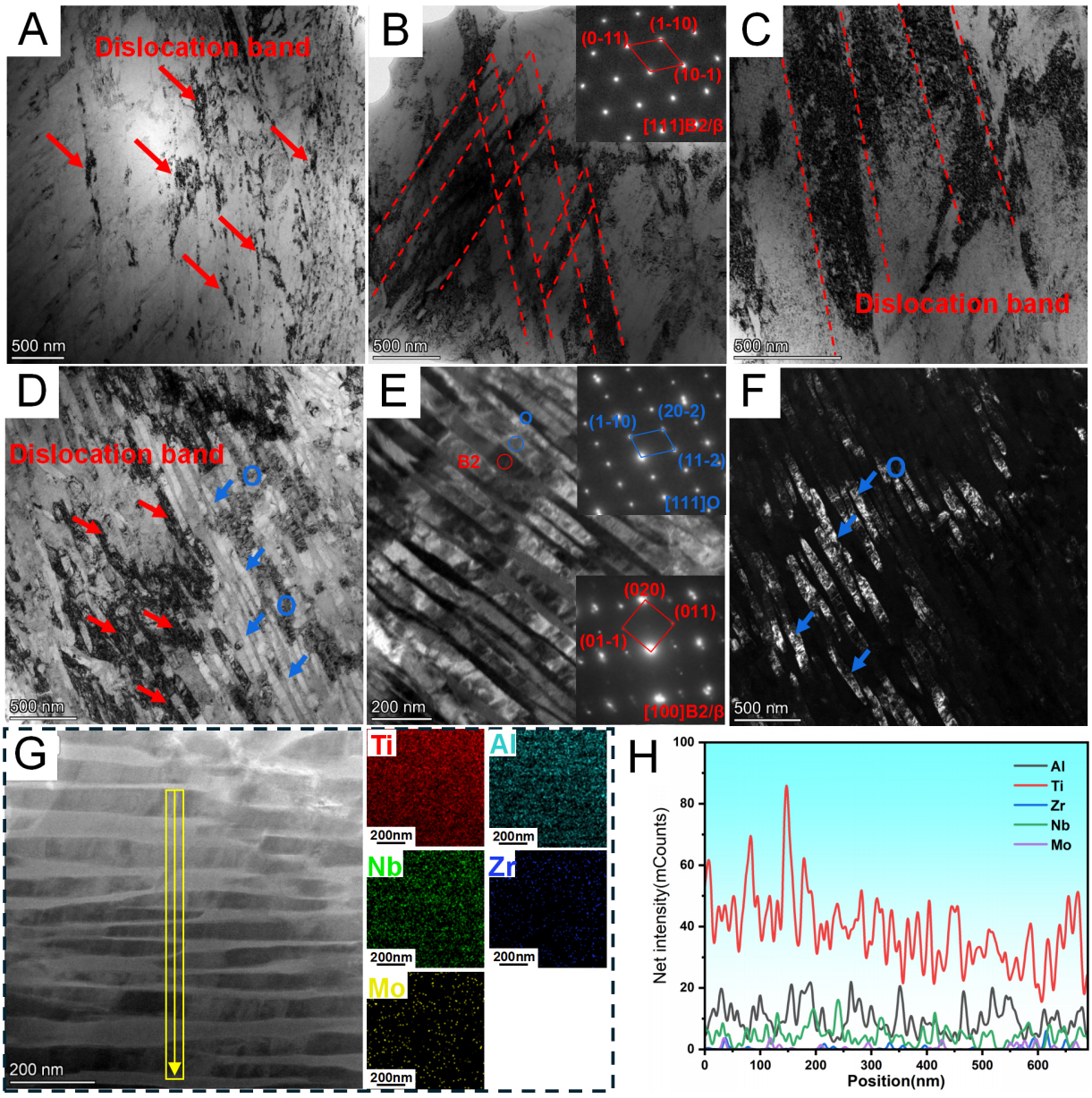


Figure 11. (A-C) Dislocation configuration of the cold-rolled microstructure; (D and E) Bright-field images, (F) dark-field image, (G) HAADF image and corresponding EDS elemental mappings, and (H) EDS line scan profiles perpendicular to the lamellae of the T880-2 sample. HAADF: High-angle annular dark-field; EDS: energy-dispersive X-ray spectroscopy.

indicates that O-phase precipitation occurred before the cold-rolling substructure had fully recovered, such that the deformation-induced defects could still influence the precipitation process. Because the B2/β-to-O transformation involves lattice rearrangement, chemical ordering, and local solute redistribution[33], cold rolling and direct aging can therefore be considered to play complementary roles. Specifically, cold rolling raises the local stored energy of the B2/β matrix and creates favorable heterogeneous nucleation sites, whereas direct aging provides the thermal activation required for structural rearrangement and solute partitioning.

The banded deformation substructures provide a directional distribution of favorable nucleation sites, while the B2/β rolling texture provides a crystallographic basis for lamellar alignment. Figure 12 presents the XRD texture analysis of the 80% cold-rolled specimen, where the X, Y, and Z directions correspond to RD, TD,

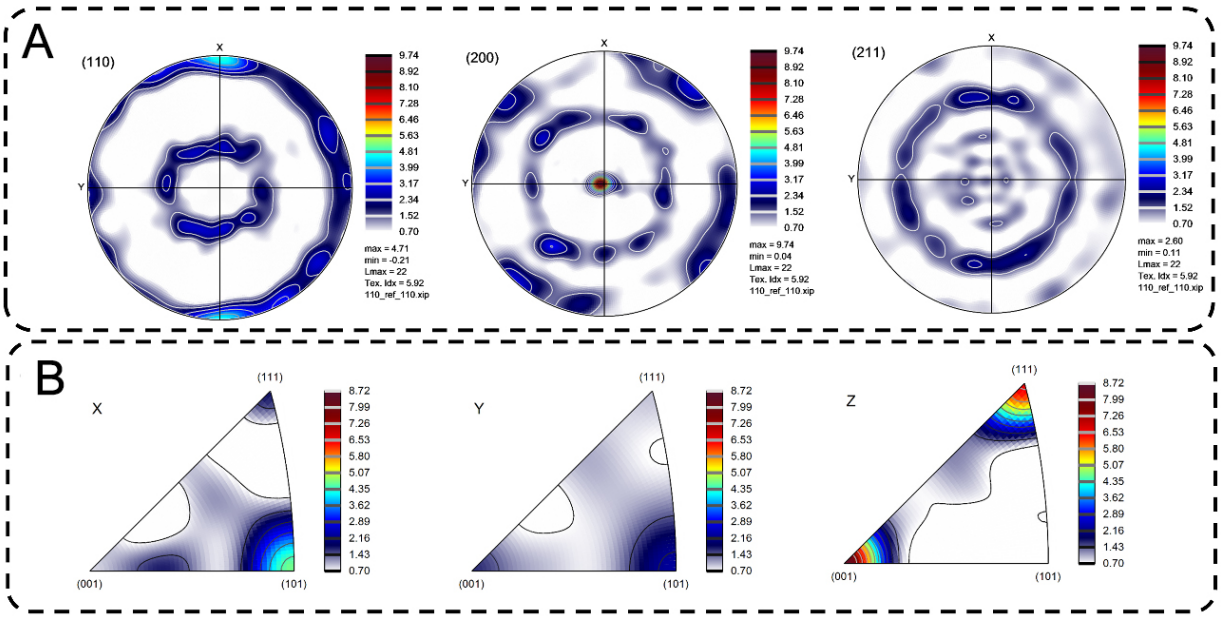


Figure 12. (A) Pole figure and (B) inverse pole figure of the alloy subjected to 80% cold rolling. The X, Y, and Z directions correspond to RD, TD, and ND, respectively. RD: Rolling direction; TD: transverse direction; ND: normal direction.

and ND, respectively. Concentrated intensity maxima appear in the B2/β pole figures in Figure 12A, indicating that the grain orientations deviate markedly from a random distribution. The inverse pole figure (IPF) in Figure 12B further shows that RD is concentrated near < 110 >, whereas ND clusters around < 001 > and < 111 >; the TD distribution is comparatively diffuse. These results confirm the development of a pronounced rolling texture in the B2/β matrix. O-phase precipitation from the B2/β parent phase is constrained by the B2/O crystallographic relationship. The concentration of parent-phase orientations therefore restricts the crystallographically favored O-phase variants and their associated habit-plane orientations to a narrower range of spatial directions. Previous studies have shown that the texture of the B2 parent phase can influence the O-phase orientation distribution through the B2 → O transformation, while preferential precipitation at deformation defects may further enhance the alignment of the O-phase lamellae[15,34].

The local stress fields associated with dislocations may also alter the relative stability of different O-phase variants. Each variant has a distinct transformation strain and therefore interacts differently with the local stress state. Variants that more effectively accommodate the local stress are energetically favored and may subsequently develop into groups of similarly aligned lamellae. Zheng *et al.*[14] found that a high dislocation density enhanced O-phase variant selection in a Ti-22Al-25Nb alloy, with the preferred variants developing into nearly parallel lamellae. Furuhara and Maki also identified the interaction between transformation strain and local defect-induced stress fields as an important origin of variant selection during diffusional phase transformations[35]. The directionally aligned lamellae observed in the present study are therefore consistent with this dislocation-assisted preferential precipitation mechanism.

The schematic in Figure 13 summarizes the proposed microstructural evolution. Cold rolling first introduces a high density of defects, banded deformation substructures, and a pronounced rolling texture in the B2/β matrix. Subsequent direct aging promotes O-phase precipitation while allowing these inherited deformation features to influence the spatial and crystallographic arrangement of the resulting lamellae. Because no high-temperature solution treatment was performed after cold rolling, the deformation-induced defects and

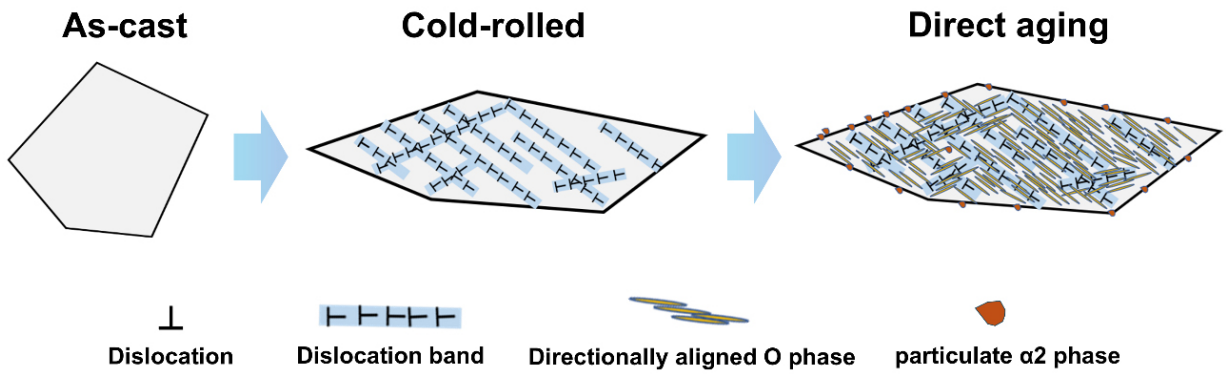


Figure 13. Schematic of O-phase precipitation mechanism during direct aging of the cold-deformed alloy.

texture were retained during the subsequent aging treatment and could continue to influence O-phase precipitation. Preservation of the cold-deformed state is therefore central to both promoting O-phase precipitation and controlling the arrangement of the resulting lamellae.

Growth and coarsening of O-phase lamellae during direct aging

Figure 14 presents the TEM characterization of T880-30. Compared with T880-2, the bright-field image in Figure 14A shows noticeably thicker O-phase lamellae and more clearly defined O-B2/β interfaces, while their preferential alignment remains evident. The dislocation density in the interlamellar B2/β regions was markedly lower, indicating substantial recovery of the cold-rolling substructure during aging. SAED established the orientation relationship of {110}B2/β||{001}O and <111>B2/β||<110>O, consistent with the relationship commonly reported for Ti_2AlNb-based alloys[36]. In the dark-field image obtained using an O-phase reflection [Figure 14D], the lamellar regions displayed strong bright contrast, clearly revealing their spatial distribution within the B2/β matrix. The HAADF image also distinguished the O-phase lamellae from the surrounding matrix, while the EDS line scan analysis revealed clear differences in the distributions of Al and Nb between the two phases.

First-principles calculations have shown that the O(001)/B2(110) interface can adopt a stable configuration with a high work of adhesion and low interfacial energy[37]. Such crystallographic matching favors stable broad faces and may help the O phase retain its lamellar morphology during subsequent coarsening. The O phase therefore evolves mainly through lamellar lengthening and thickening, accompanied by the disappearance of some finer lamellae, rather than through a general transition to equiaxed particles. As a result, the directional alignment established during the early stage of direct aging in the cold-rolled state is retained during further aging.

Comparison with T880-2 further indicates that solute redistribution accompanies both the early formation and subsequent growth of the O phase. Lamellar growth is therefore not a simple advance of the interface, but involves the coupled processes of interface migration and solute diffusion. During the early stage of aging, the stored energy introduced by cold rolling and the chemical free-energy difference between the O phase and the supersaturated B2/β matrix provide driving force for lamellar formation and growth. As dislocations progressively recover and solute partitioning between O and B2/β becomes established, the contributions from deformation-induced stored energy and local concentration gradients are gradually reduced. Differences in thermodynamic stability among lamellae of different sizes then become increasingly important.

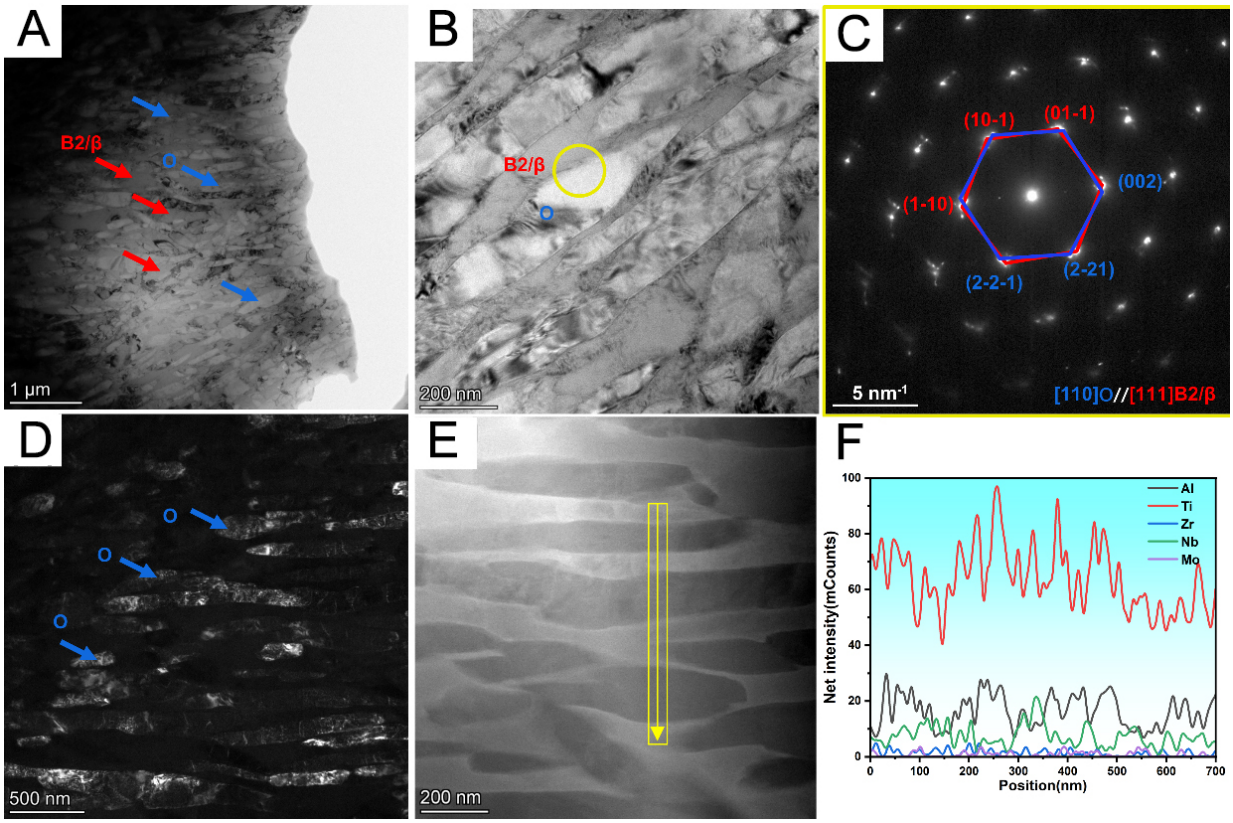


Figure 14. (A and B) Bright-field images, (C) SAED pattern taken at the B2/β-O interface, (D) dark-field image of the O phase, (E) HAADF image, and (F) EDS line scan analysis perpendicular to the lamellae of the T880-30 sample. SAED: Selected-area electron diffraction; HAADF: high-angle annular dark-field; EDS: energy-dispersive X-ray spectroscopy.

Fine O-phase lamellae contain a larger proportion of tip and edge regions, resulting in a higher interfacial-energy contribution and greater susceptibility to shrinkage or dissolution. Solute released during this process diffuses through the B2/β matrix and is redistributed to larger lamellae, allowing them to thicken or lengthen further[38]. This competitive coarsening process consequently decreases the number of lamellae and widens the intervening B2/β channels. Previous studies have similarly reported that the early growth of lamellar O phase in Ti_2AlNb alloys is associated with deformation-induced stored energy and concentration gradients between O and B2/β, whereas the growth rate decreases as the stored energy is released and the concentration gradients diminish.

Aging temperature affects both atomic diffusion and the O/B2 phase equilibrium. Raising the temperature accelerates solute diffusion and interface migration, thereby facilitating both the dissolution of finer lamellae and the continued growth of larger ones. At the same time, the equilibrium fraction of the O phase decreases as the temperature moves toward the B2/β-stable regime, favoring a larger proportion of B2/β[39]. The transition from a fine, dense lamellar structure to a coarse, sparse one cannot therefore be attributed solely to accelerated lamellar growth. Instead, it results from the combined effects of competitive coarsening and temperature-dependent adjustment of the O/B2 phase fractions. At higher temperatures, some fine O-phase lamellae dissolve back into the B2/β matrix, while the relatively stable lamellae remain and continue to grow, ultimately producing a microstructure composed of coarsened O-phase lamellae and widened B2/β channels[40].

Strengthening and plastic deformation mechanisms

The results presented above show that the cold-rolling substructure mainly affects the early precipitation and arrangement of the O phase, whereas the direct-aging temperature further modifies the size and spacing of the O-phase lamellae and the dislocation substructure retained in the B2/β matrix. These microstructural factors strongly influence the strength and ductility of the alloy. Although T840-30, T880-30, and T920-30 share the same nominal composition and cold-rolling reduction, variations in aging temperature also alter the O-phase fraction, O/B2 interface density, B2/β channel width, and elemental partitioning. Consequently, the contributions from other strengthening mechanisms cannot be reliably separated or assumed to remain constant among the three conditions. Based on the dislocation densities and O-phase lamellar parameters determined for these specimens, the corresponding changes in dislocation strengthening and O-phase obstacle strengthening were estimated to evaluate their contributions to the variation in strength with aging temperature.

The dislocation-strengthening contribution was calculated using the classical Taylor relation[41]:

$$\Delta\sigma_\rho = M\alpha Gb\sqrt{\rho} \tag{2}$$

where M is the Taylor factor, α is the dislocation-strengthening coefficient, G is the shear modulus of the B2/β phase, b is the Burgers vector, and ρ is the dislocation density. The calculations used M = 3.06, α = 0.30, and G = 39.3 GPa. The value of M corresponds to the conventional average Taylor factor for a polycrystalline bcc material, while α = 0.30 falls within the commonly adopted range for dislocation interactions[42,43]. A constant G of 39.3 GPa was used because the dislocation densities were determined from the B2/β diffraction peaks and the present calculation therefore describes dislocation strengthening within the B2/β matrix. Dislocation densities were estimated from XRD peak broadening using Williamson-Hall analysis combined with the Williamson-Smallman relation[44,45]. The estimated dislocation densities for T840-30, T880-30, and T920-30 were approximately 2.10×10^{15}, 5.82×10^{14} and 2.16×10^{14} m^{-2} respectively, corresponding to dislocation-strengthening contributions of 463, 244, and 148 MPa. The monotonic decrease with increasing aging temperature reflects progressive recovery of the cold-rolling substructure. The particularly large reduction between T840-30 and T880-30 indicates that dislocation recovery became substantially more extensive when the aging temperature was increased to 880 ℃.

Fine O-phase lamellae also impede dislocation motion in the B2/β matrix. An Orowan-type obstacle model was used to estimate the change in strengthening caused by variations in lamellar thickness and spacing[46,47]:

$$\Delta\sigma_O = \frac{0.4MGb}{\pi\sqrt{1-\nu}\lambda}\ln\left(\frac{d}{b}\right) \tag{3}$$

where ν is Poisson's ratio, d is the effective thickness of the O-phase lamellae, and λ is the effective spacing between adjacent lamellae. The calculated O-phase strengthening contributions were approximately 372, 236, and 128 MPa for T840-30, T880-30, and T920-30, respectively. Because the three specimens had the same composition and cold-rolled starting condition, application of the same model provides a consistent basis for comparing the spacing-dependent O-phase strengthening among the aging conditions. In this expression, lamellar thickness enters logarithmically, whereas spacing appears in the denominator. An increase in spacing therefore has a more direct effect on the reduction in O-phase strengthening. As the O phase evolves from a fine, closely spaced arrangement to a coarser and more widely spaced one, a gliding dislocation encounters fewer lamellae over a given slip distance, thereby reducing the resistance to dislocation motion and the associated strengthening contribution[48].

The high dislocation density and closely spaced O-phase lamellae in T840-30 imposed strong constraints on dislocation motion, resulting in the highest strength. The narrow B2/β channels, however, restricted the space available for dislocation glide and plastic accommodation. The accumulation of dislocations near the interfaces suggests that local plastic strain was less readily accommodated across adjacent regions, thereby increasing local stress concentration. At 880 °C, dislocation recovery and moderate coarsening of the O phase reduced the overall resistance to deformation, while the wider B2/β channels facilitated dislocation glide and strain accommodation. Meanwhile, the O-phase lamellae remained effective barriers to dislocation motion[49]. The deformation response therefore shifted from one dominated by a high density of obstacles to a better balance between O-phase strengthening and plastic accommodation in the B2/β matrix.

Fracture morphologies and post-tensile TEM observations provide further evidence for this transition, as shown in Figures 15 and 16. T840-30 exhibited relatively small and shallow dimples, together with locally flat regions, whereas more fully developed dimples formed in T880-30. After tensile deformation [Figure 16], numerous dislocations were present within the B2/β channels of T880-30. Some dislocations piled up or became tangled near the O/B2 interfaces, but the interfaces remained continuous. Plastic deformation in Ti_2AlNb alloys is generally accommodated primarily by the B2 phase, which offers more available slip systems, while the O phase contributes to strengthening by impeding dislocation motion. The post-tensile dislocation structure is consistent with this complementary role of the two phases: the B2/β channels provide the main pathways for dislocation glide, the O-phase lamellae remain effective obstacles, and the continuous interfaces remain intact despite local dislocation accumulation, suggesting resistance to premature interfacial decohesion.

At an aging temperature of 920 °C, both dislocation strengthening and O-phase obstacle strengthening were substantially reduced. The wider and more continuous B2/β regions imposed weaker geometric constraints on dislocation glide, allowing plastic deformation to be accommodated over a larger microstructural volume. Consequently, T920-30 achieved the highest uniform elongation and exhibited more pronounced ductile-fracture features. At the same time, the concurrent reductions in residual dislocation density and O-phase barrier density lowered the resistance to dislocation motion and yielding.

At 650 °C, increased thermal activation facilitates dislocation motion and reduces the stress required to overcome local obstacles. All three specimens therefore exhibited lower ultimate tensile strengths than at room temperature. However, the strength followed the same ranking as at room temperature, decreasing from T840-30 to T880-30 and T920-30, indicating that the retained dislocation substructure and O-phase lamellae continued to contribute to strengthening at 650 °C. The lamellar O phase continues to impede dislocation motion in the B2/β matrix and thus provides an important strengthening contribution at elevated temperatures[50]. T880-30 retained an ultimate tensile strength of 943 MPa at 650 °C while also exhibiting good room-temperature ductility, thereby providing a favorable combination of room-temperature strength-ductility balance and elevated-temperature strength.

CONCLUSION

In this study, four Ti_2AlNb-based alloys, Ti-20Al-23Nb and Ti-20Al-(23-x)Nb-xZr-0.5Mo (x = 2, 4, 6), were designed and evaluated. Ti-20Al-21Nb-2Zr-0.5Mo was selected based on its as-cast microstructure and room-temperature tensile properties and was subsequently subjected to 80% cold rolling and direct aging. O-phase precipitation, lamellar evolution, and the associated tensile behavior at room temperature and 650 °C were investigated. The main conclusions are as follows.

(1) The as-cast microstructure of all four alloys consisted predominantly of the B2/β phase. As Zr progressively replaced Nb, the average grain size decreased from 176 to 110 μm, while the tensile properties varied non-monotonically. Ti-20Al-21Nb-2Zr-0.5Mo exhibited the most favorable strength-ductility balance,

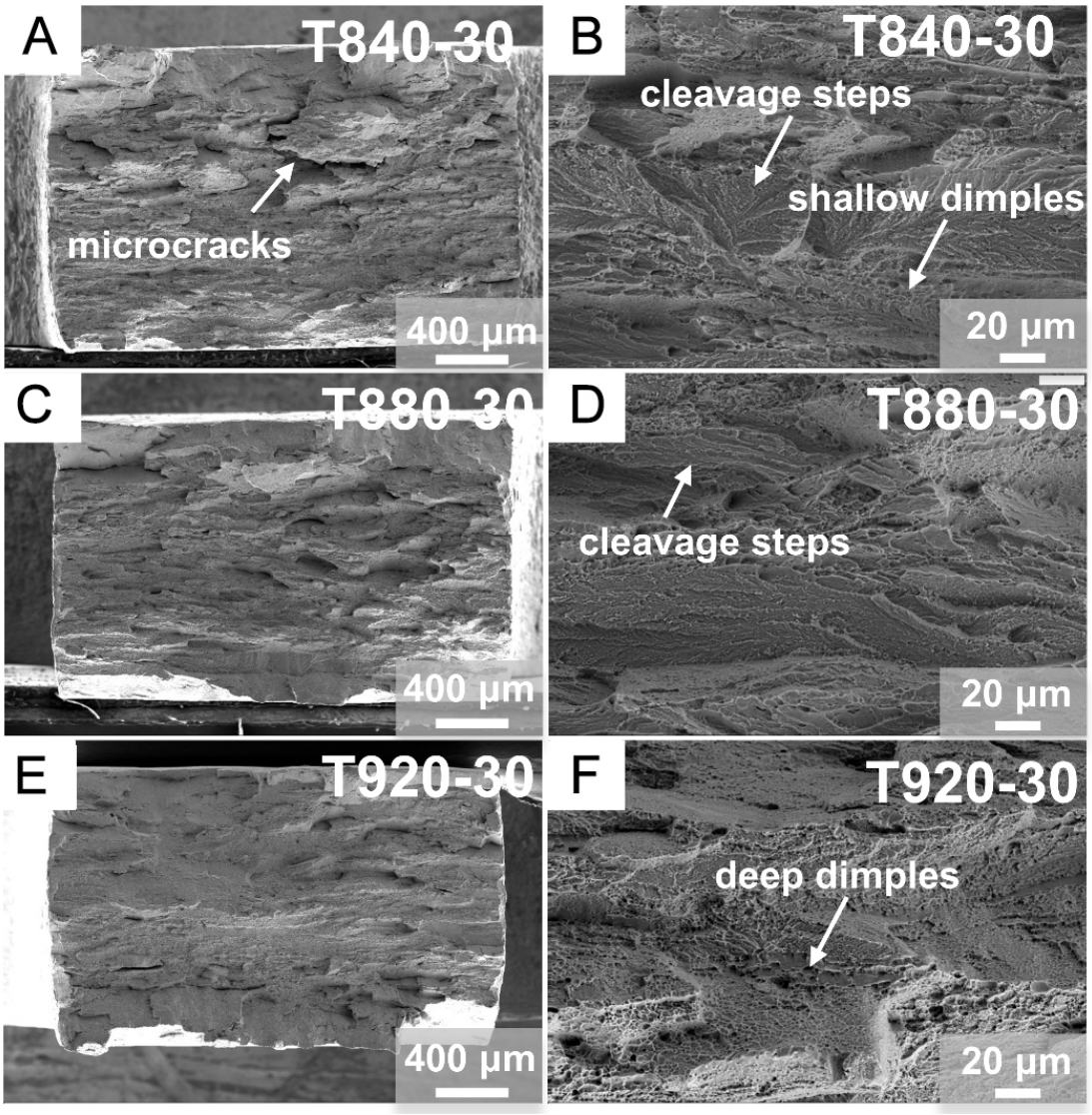


Figure 15. Room-temperature tensile fracture surfaces of the (A and B) T840-30, (C and D) T880-30, and (E and F) T920-30 samples.

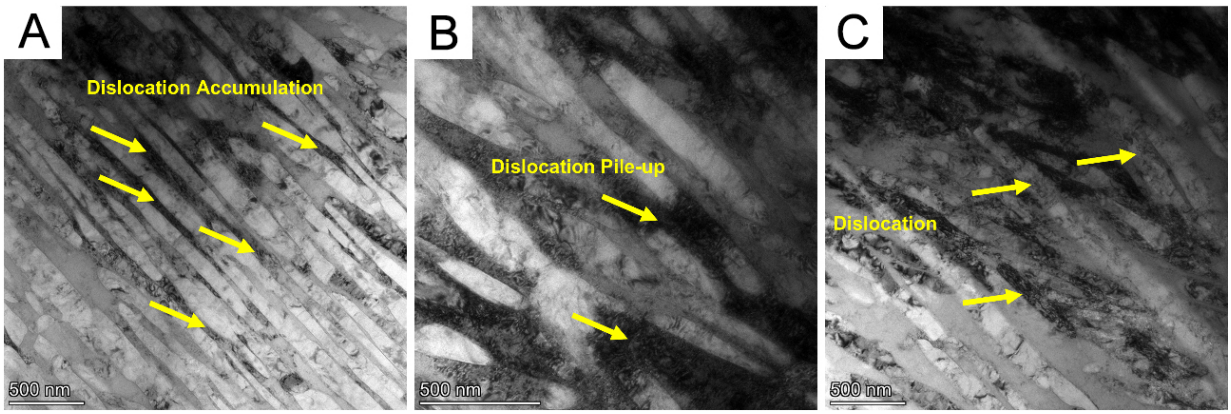


Figure 16. Dislocation configurations in the T880-30 specimen after room-temperature tensile testing: (A) low-magnification and (B) high-magnification images in the B2/β phase, and (C) images in the O phase.

with an ultimate tensile strength of 894 MPa and an uniform elongation of 13.2%.

(2) Cold rolling introduced a high density of dislocations, banded substructures, and a pronounced rolling texture of the B2/β matrix. After direct aging at 880 °C for 2 min, preferentially aligned O-phase lamellae formed with an area fraction of 45.4%, substantially higher than that in the undeformed specimen. This comparison demonstrates that prior cold rolling accelerated early O-phase precipitation. The enhanced precipitation is associated with the retained deformation substructure, while the preferential alignment is attributed to the combined effects of local defect-induced stress fields and the B2/β rolling texture.

(3) At 880 °C, longer aging increased the interlamellar spacing more markedly than the lamellar thickness, while the O-phase area fraction changed only slightly. Higher aging temperatures coarsened the O-phase lamellae, reduced their area fraction, and widened the B2/β channels, indicating partial dissolution of the O phase. The preferred alignment remained evident after coarsening. From 840 to 920 °C, the strength and model-estimated contributions from dislocation and O-phase obstacle strengthening decreased, while the uniform elongation increased from 4.2% to 12.3%. T880-30 attained a yield strength of 1,046 MPa, an ultimate tensile strength of 1,223 MPa, and an uniform elongation of 9.6% at room temperature, while retaining an ultimate tensile strength of 943 MPa at 650 °C.

(4) Post-tensile TEM observations showed that dislocations were concentrated mainly within the B2/β channels and accumulated near the O/B2 interfaces. Together with the tensile results, these observations support a mechanism in which the residual dislocations and O-phase lamellae contribute to strength, while the continuous B2/β channels accommodate plastic strain.

Overall, direct aging after cold rolling preserves deformation-induced substructures and texture without an intervening solution treatment, thereby promoting early O-phase precipitation and preferential lamellar alignment while enabling control of the lamellar dimensions and B2/β channel width, ultimately providing a favorable balance of strength and ductility together with high elevated-temperature strength.

DECLARATIONS

Authors' contributions

Writing - review & editing, writing - original draft, methodology, data curation: Zhang, X.
Validation, supervision: Wu, Y.; Wang, W. Y.; Liu, X.
Methodology, investigation: Li, C.
Validation, supervision, funding acquisition: Hui, X.

Availability of data and materials

The data supporting the findings of this study are available within this Article and its Supplementary Materials. Further data are available from the corresponding authors upon request.

AI and AI-assisted tools statement

Not applicable.

Financial support and sponsorship

This work was supported by the National Natural Science Foundation of China (Nos. U22A20105 and 52373278).

Conflicts of interest

All authors declared that there are no conflicts of interest.

Ethical approval and consent to participate

Not applicable.

Consent for publication

Not applicable.

Copyright
© The Author(s) 2026.

Supplementary Materials
Supplementary Materials

REFERENCES

1. Banerjee, D. The intermetallic Ti_2AlNb. *Prog. Mater. Sci.* **1997**, *42*, 135-58. DOI
2. Hu, R.; Zhang, K.; Zou, H.; et al. Research progress on Ti_2AlNb-based alloys and composites for aerospace applications. *J. Alloys. Compd.* **2025**, *1021*, 179701. DOI
3. Guo, Y.; Liu, Y.; Wu, Y.; Cao, H.; Mo, D.; Morandini, M. Design optimization and burst speed prediction of a Ti_2AlNb blisk. *Int. J. Aerosp. Eng.* **2021**, *2021*, 1-12. DOI
4. Fu, Y.; Su, Z. Elemental composition, phase diagram, microstructure, fabrication processes, and mechanical properties of Ti_2AlNb alloy: a review. *J. Mater. Eng. Perform.* **2024**, *33*, 12819-46. DOI
5. Li, N.; Yu, S.; Liu, J.; et al. Dynamic spheroidization and synergistic evolution of the lamellar microstructure in the Ti_2AlNb alloy during hot deformation below the B2-transus temperature. *J. Alloys. Compd.* **2026**, *1076*, 189312. DOI
6. Zhou, M.; Bu, Z.; Zhou, Y.; et al. The effect of primary and secondary O phase on the mechanical properties and deformation behavior of Ti_2AlNb alloy. *J. Alloys. Compd.* **2025**, *1032*, 181160. DOI
7. Germann, L.; Banerjee, D.; Guédou, J.; Strudel, J. Effect of composition on the mechanical properties of newly developed Ti_2AlNb-based titanium aluminide. *Intermetallics* **2005**, *13*, 920-4. DOI
8. Liu, T.; Li, X.; Wei, B. The influences of heat treatment on the microstructure and mechanical properties of rolled Ti_2AlNb. *Metals* **2023**, *13*, 886. DOI
9. Jia, Z.; Zhang, Y.; Yu, Q.; et al. Enhancing mechanical properties of (Ti, Nb)B/Ti_2AlNb composites via hot extrusion: microstructural evolution, strengthening and fracture mechanisms. *Mater. Sci. Eng. A.* **2026**, *962*, 150169. DOI
10. Zhou, Y.; Zhou, M.; Bu, Z.; Huang, X.; Li, J. Effect of aging time on microstructure and mechanical properties of Ti_2AlNb alloy. *Mater. Lett.* **2026**, *422*, 141300. DOI
11. Wang, W.; Zeng, W.; Xue, C.; Liang, X.; Zhang, J. Designed bimodal size lamellar O microstructures in Ti_2AlNb based alloy: microstructural evolution, tensile and creep properties. *Mater. Sci. Eng. A.* **2014**, *618*, 288-94. DOI
12. Zou, Y.; Zhang, X.; Zhang, W.; Han, F.; Han, J.; Jia, Y. Effect of solution temperature on the microstructure and properties of Ti_2AlNb alloy sheets. *Intermetallics* **2026**, *192*, 109217. DOI
13. Tang, W.; Shao, B.; Zong, Y. The effect of 0.02-0.37 strain on the precipitation law of O phase colonies in Ti_2AlNb-based alloy during aging. *J. Mater. Res. Technol.* **2023**, *22*, 89-96. DOI
14. Zheng, Y.; Zeng, W.; Li, D.; et al. Orthorhombic precipitate variant selection in a Ti_2AlNb based alloy. *Mater. Des.* **2018**, *158*, 46-61. DOI
15. Wu, Y.; Kou, H.; Tang, B.; Liu, D.; Li, J.; Li, J. O phase precipitation and variant selection in Ti-22Al-25Nb alloy during the hot shear spinning. *Adv. Eng. Mater.* **2018**, *20*, 1800153. DOI
16. Wei, J.; Jia, Y.; Zhang, Y.; et al. Effect of hot rolling process on the evolution of microstructure and mechanical properties of Ti_2AlNb-based alloy foil during cold rolling. *Mater. Charact.* **2024**, *210*, 113784. DOI
17. Erndt-Marino, J. D.; Becerra-Bayona, S.; McMahon, R. E.; Goldstein, A. S.; Hahn, M. S. Cell layer-electrospun mesh composites for coronary artery bypass grafts. *J. Biomed. Mater. Res. A.* **2016**, *104*, 2200-9. DOI PubMed PMC
18. Guo, Y.; Niu, J.; Cao, J.; Sun, Z.; Dan, Z.; Chang, H. Relative strength of β phase stabilization by transition metals in titanium alloys: the Mo equivalent from a first principles study. *Mater. Today. Commun.* **2023**, *35*, 106123. DOI
19. He, Y.; Hu, R.; Luo, W.; et al. Microstructure and mechanical properties of a new Ti_2AlNb-based alloy after aging treatment. *Rare. Metals.* **2018**, *37*, 942-51. DOI
20. Wang, W.; Zeng, W.; Xue, C.; Liang, X.; Zhang, J. Microstructure control and mechanical properties from isothermal forging and heat treatment of Ti-22Al-25Nb (at.%) orthorhombic alloy. *Intermetallics* **2015**, *56*, 79-86. DOI
21. Wang, W.; Zeng, W.; Liu, Y.; Xie, G.; Liang, X. Microstructural evolution and mechanical properties of Ti-22Al-25Nb (At.%) orthorhombic alloy with three typical microstructures. *J. Mater. Eng. Perform.* **2018**, *27*, 293-303. DOI
22. Wang, W.; Zeng, W.; Li, D.; Zhu, B.; Zheng, Y.; Liang, X. Microstructural evolution and tensile behavior of Ti_2AlNb alloys based α_2-phase decomposition. *Mater. Sci. Eng. A.* **2016**, *662*, 120-8. DOI

23. Sui, X.; Wang, G.; Liu, Q.; Liu, Y.; Chen, Y. Fabricating Ti_2AlNb sheet with tensile strength higher than 1500 MPa by hot packed rolling spark-plasma-sintered pre-alloyed Ti_2AlNb powder at the B2+O phase field. *J. Alloys. Compd.* **2021**, *876*, 160110. DOI
24. Zhang, H.; Wu, Y.; Zhang, J.; Liu, Y. Synergistic effect of B2 phase and O phase in hot-rolled Ti_2AlNb alloy and its influences on mechanical properties. *J. Mater. Res. Technol.* **2024**, *30*, 2004-17. DOI
25. Tang, Y.; Zhang, Y.; Liu, Y. Numerical and experimental investigation of laser additive manufactured Ti_2AlNb-based alloy. *J. Alloys. Compd.* **2017**, *727*, 196-204. DOI
26. Zhou, Y.; Wang, D.; Song, L.; et al. Effect of heat treatments on the microstructure and mechanical properties of Ti_2AlNb intermetallic fabricated by selective laser melting. *Mater. Sci. Eng. A.* **2021**, *817*, 141352. DOI
27. Polozov, I.; Gracheva, A.; Popovich, A. Processing, microstructure, and mechanical properties of laser additive manufactured Ti_2AlNb-based alloy with carbon, boron, and yttrium microalloying. *Metals* **2022**, *12*, 1304. DOI
28. Chen, Q.; Xu, L.; Zhang, Y.; et al. Additive manufacturing Ti-22Al-25 Nb alloy with excellent high temperature tensile properties by electron beam powder bed fusion. *Addit. Manuf.* **2024**, *86*, 104236. DOI
29. Jia, J.; Liu, W.; Xu, Y.; et al. Microstructure evolution, B2 grain growth kinetics and fracture behaviour of a powder metallurgy Ti-22Al-25Nb alloy fabricated by spark plasma sintering. *Mater. Sci. Eng. A.* **2018**, *730*, 106-18. DOI
30. Jia, J.; Zhang, K.; Jiang, S. Microstructure and mechanical properties of Ti-22Al-25Nb alloy fabricated by vacuum hot pressing sintering. *Mater. Sci. Eng. A.* **2014**, *616*, 93-8. DOI
31. Wang, G.; Yang, J.; Jiao, X. Microstructure and mechanical properties of Ti-22Al-25Nb alloy fabricated by elemental powder metallurgy. *Mater. Sci. Eng. A.* **2016**, *654*, 69-76. DOI
32. Fu, Y.; Cui, Z. Effects of plastic deformation and aging treatment on phase precipitation in Ti_2AlNb alloy. *J. Mater. Eng. Perform.* **2022**, *31*, 2633-43. DOI
33. Sadi, F.; Servant, C. On the B2→O phase transformation in Ti-Al-Nb alloys. *Mater. Sci. Eng. A.* **2003**, *346*, 19-28. DOI
34. Zhang, P.; Zeng, W.; Ma, H.; et al. Research on tensile anisotropy of Ti-22Al-25Nb alloy isothermally forged in B2 phase region related with texture and variant selection. *Mater. Charact.* **2023**, *201*, 112899. DOI
35. Furuhara, T.; Maki, T. Variant selection in heterogeneous nucleation on defects in diffusional phase transformation and precipitation. *Mater. Sci. Eng. A.* **2001**, *312*, 145-54. DOI
36. Bendersky, L.; Boettinger, W.; Roytburd, A. Coherent precipitates in the b.c.c./orthorhombic two-phase field of the Ti Al Nb system. *Acta. Metall. Mater.* **1991**, *39*, 1959-69. DOI
37. Wang, A.; Liu, P.; Xie, J.; Ma, D.; Mao, Z. First-principles investigation on the atomic structure, stability and electronic property of O(001)/B2(110) interface in Ti_2AlNb alloys. *J. Alloys. Compd.* **2020**, *817*, 152734. DOI
38. Zhou, X.; Liu, J.; Zhang, S.; et al. Microstructure evolution and coarsening behavior of precipitated O phase in Ti-22Al-24Nb-0.5Mo (at. %) alloy during the heat treatment. *J. Mater. Res. Technol.* **2023**, *27*, 4236-47. DOI
39. Tumminello, S.; Gussone, J.; Fries, S. G.; et al. Precipitation simulations of the O-phase in Ti_2AlNb alloys processed by laser powder bed fusion. *Adv. Eng. Mater.* **2026**, *28*, e70963. DOI
40. Zhang, H.; Yan, N.; Liang, H.; Liu, Y. Phase transformation and microstructure control of Ti_2AlNb-based alloys: a review. *J. Mater. Sci. Technol.* **2021**, *80*, 203-16. DOI
41. Bailey, J. E.; Hirsch, P. B. The dislocation distribution, flow stress, and stored energy in cold-worked polycrystalline silver. *Philos. Mag.* **1960**, *5*, 485-97. DOI
42. Stoller, R.; Zinkle, S. On the relationship between uniaxial yield strength and resolved shear stress in polycrystalline materials. *J. Nucl. Mater.* **2000**, *283-287*, 349-52. DOI
43. Mughrabi, H. The α-factor in the Taylor flow-stress law in monotonic, cyclic and quasi-stationary deformations: dependence on slip mode, dislocation arrangement and density. *Curr. Opin. Solid. State. Mater. Sci.* **2016**, *20*, 411-20. DOI
44. Williamson, G. K.; Smallman, R. E. III. Dislocation densities in some annealed and cold-worked metals from measurements on the X-ray debye-scherrer spectrum. *Philos. Mag.* **1956**, *1*, 34-46. DOI
45. Williamson, G.; Hall, W. X-ray line broadening from filed aluminium and wolfram. *Acta. Metall.* **1953**, *1*, 22-31. DOI
46. Zhang, Z.; Chen, D. Consideration of Orowan strengthening effect in particulate-reinforced metal matrix nanocomposites: a model for predicting their yield strength. *Scr. Mater.* **2006**, *54*, 1321-6. DOI
47. Zheng, Y.; Zeng, W.; Zhang, P.; et al. Anti-correlation between solution strengthening and precipitation strengthening in lamellar O microstructures of a Ti_2AlNb based alloy. *J. Alloys. Compd.* **2020**, *847*, 156470. DOI
48. Zhu, Y.; Song, J.; Li, Z.; et al. Study on the relationship between microstructure and tensile properties of Ti-22Al-25Nb alloy and the establishment of quantitative models. *J. Alloys. Compd.* **2025**, *1020*, 179374. DOI

49. Zhang, P.; Zeng, W.; Zhang, F.; et al. In-situ investigation of tensile anisotropy mechanism in an advanced Ti_2AlNb-based alloy associated with CRSS ratio and damage model. *Mater. Sci. Eng. A.* **2024**, *890*, 145894. DOI
50. Shao, B.; Tang, W.; Guo, S.; Zong, Y.; Shan, D.; Guo, B. Investigation of the O phase in the Ti-22Al-25Nb alloy during deformation at elevated temperatures: plastic deformation mechanism and effect on B2 grain boundary embrittlement. *Acta. Mater.* **2023**, *242*, 118467. DOI

Disclaimer/Publisher's Note: All statements, opinions, and data contained in this publication are solely those of the individual author(s) and contributor(s) and do not necessarily reflect those of OAE and/or the editor(s). OAE and/or the editor(s) disclaim any responsibility for harm to persons or property resulting from the use of any ideas, methods, instructions, or products mentioned in the content.


© The Author(s) 2026. Open Access This article is licensed under a Creative Commons Attribution 4.0 International License (https://creativecommons.org/licenses/by/4.0/), which permits unrestricted use, sharing, adaptation, distribution and reproduction in any medium or format, for any purpose, even commercially, as long as you give appropriate credit to the original author(s) and the source, provide a link to the Creative Commons license, and indicate if changes were made.